Enhancing Cycling Stability In Symmetric Solid-State Na-Ion Batteries Via Composite Polymer Buffer Layer

Saurabh Sharma, Sandipan Bhattacharyya, Ravi P. Srivastava, Sourabh Shyamal, Mohd Aman, and Shobit Omar*

Solid-state sodium-ion batteries (SSIBs) represent an advanced energy storage technology, offering superior safety, thermal stability, and robust long-term cycling performance. However, their practical deployment is critically constrained by the low ionic conductivity of solid electrolytes (SEs) and pronounced interfacial instability—stemming from poor physical contact between the electrode and SE, as well as parasitic reactions involving metallic sodium and liquid electrolyte-based interfacial modifiers. In this work, the development of a composite polymer buffer layer (CPBL) is reported as an interfacial modifier to establish stable and intimate contact at the electrode-SE interface. Integrated into a symmetric full-cell configuration using Fe-doped $Na_3V_2(PO_4)_3$ electrodes and NASICON-type ceramic electrolyte, the SSIB delivers a discharge capacity of $\approx 45\ mAh\,g^{-1}$ (theoretical capacity $\approx 58.8\ mAh\,g^{-1}$) at C/5, with 89% capacity retention over 200 cycles at 25 °C. Notably, the SSIB assembly is carried out in ambient conditions without the need for an inert atmosphere. The enhanced electrochemical performance is attributed to the synergistic effects of improved ionic conductivity and superior interfacial contact, which collectively facilitate efficient Na^+ transport across the electrode-SE interface. These findings underscore the potential of CPBL to overcome interfacial challenges in SSIBs and advance the development of safe, high-performance, and sustainable sodium-based energy storage systems.

1. Introduction

The growing global demand for energy is accelerating a decisive shift toward renewable sources. However, their intermittent nature necessitates the development of high-performance energy storage systems to stabilize supply and demand and ensure seamless integration into the energy grid.[1] Among the various energy storage technologies, electrochemical storage via batteries remains the most practical solution, offering high efficiency and zero greenhouse gas emissions.[2] While lithium-ion batteries (LIBs) and lead-acid batteries dominate the current market, their reliance on scarce and toxic materials has prompted the search for sustainable alternatives. Sodium-ion batteries (SIBs) have emerged as a promising candidate owing to the abundance, low-cost raw materials, and the environmental benignity of sodium, despite certain compromises in energy and power density compared to LIBs.[3,4]

While SIBs hold significant potential, several challenges must be addressed before they can be commercialized. Traditional SIBs are typically assessed in half-cell configurations using metallic sodium anodes; however, safety concerns arise due to dendrite formation and the instability of the solid electrolyte interphases (SEI).[5] Full-cell configurations employing alternative anode materials, such as hard carbon or metal-based compounds, face significant challenges due to capacity imbalance and the inherent complexity of electrode fabrication. Hard carbon anodes, while used, operate dangerously close to the sodium plating potential, raising serious safety concerns such as dendrite formation and thermal runaway.[6] Symmetrical full-cell configurations provide key advantages over conventional full cells, such as: i) minimal volume change during cycling and ii) a streamlined electrode fabrication process, which enhances operational uniformity, making them attractive for scalable energy storage applications.[7,8] However, when paired with conventional organic liquid electrolytes (OLE), these systems are constrained by several critical drawbacks, including high flammability, narrow electrochemical stability windows, and the potential for electrolyte leakage—all of which pose serious safety and durability concerns.[9] Solid electrolytes (SEs) effectively address these limitations, positioning symmetric solid-state SIBs (SSIBs) as a safer, more stable, and highly promising next-generation energy storage technology.[10]

The design of an efficient symmetric SSIB critically depends on the material selection of compatible electrodes and SE materials. Among the various electrode candidates, $Na_3V_2(PO_4)_3$ (NVP), a NASICON-type redox active material, has garnered considerable attention owing to its excellent cycling stability and favorable electrochemical characteristics.[11] Importantly, NVP possesses

S. Sharma, S. Bhattacharyya, S. Shyamal, M. Aman, S. Omar
Department of Materials Science & Engineering
Indian Institute of Technology Kanpur
Kanpur 208016, India
E-mail: somar@iitk.ac.in

R. P. Srivastava
Department of Materials Engineering
Indian Institute of Technology Jodhpur
Jodhpur 342037, India

R. P. Srivastava
Rishabh Centre for Research and Innovation in Clean Energy
Indian Institute of Technology Jodhpur
Jodhpur 342037, India

Batteries & Supercaps

Research Article
doi.org/10.1002/batt.202500372

Chemistry
Europe
European Chemical
Societies Publishing

two distinct redox couples: V^{4+}/V^{3+} at 3.4 V versus Na^+/Na,[12] and V^{3+}/V^{2+} at 1.6 V versus Na^+/Na.[13] This dual activity enables its use as a bipolar electrode, paving the way for the design of symmetrical SSIB, which can deliver a stable single voltage plateau around 1.8 V and significant specific capacity.[14] However, its poor electronic conductivity has been a major bottleneck to achieving a long-term cycling performance at high current rates. The major strategies attempted to deal with this challenge have been: i) aliovalent ion doping and ii) incorporation of carbonaceous electrical conducting material.[15,16]

In addition to electrode materials, the SE plays a vital role in the performance of symmetric SSIBs. NASICON-structured SEs, such as $Na_3Zr_2Si_2PO_{12}$ (NZSP), are particularly attractive due to their robust chemical stability and moderate ionic conductivity of ≈0.6 mS/cm at room temperature (RT).[17] Aliovalent doping and optimization of the Si/P molar ratio have been shown to significantly enhance Na^+ conductivity in NZSP, thereby improving the reversibility of the electrochemical processes.[18] Recently, Chakraborty et al.[19] synthesized $Na_{3\cdot456}Zr_{1\cdot872}Mg_{0\cdot128}Si_{2\cdot2}P_{0\cdot8}O_{12}$ (Mg-doped NZSP) with an impressive ionic conductivity of 3.2 mS.cm^{-1} at RT. The study also demonstrated working of symmetric SSIB with $Na_{3\cdot1}V_2P_{2\cdot9}Si_{0\cdot1}O_{12}$ (NVPS$_{0\cdot1}$) electrodes, which delivered a discharge capacity around 70 mAh g^{-1} discharge capacity at a C/10 current over 70 cycles. However, the incorporation of a small amount of OLE at the electrode-SE interface compromised the solid-state nature of the cell, complicated processing (requiring assembling under an inert atmosphere), and reintroduced safety concerns. Moreover, the use of OLE also opens the possibility of parasitic reactions that lead to the formation of an unstable SEI, affecting long-term stability.[20] Thus, a different approach is required to create a stable and sustainable interface, resulting in improved long-term SSIB performance.

To date, numerous strategies have been explored to mitigate interfacial challenges in SSIBs, including spark plasma sintering, engineered composite electrode architectures, and wet chemical infiltration techniques.[21–24] However, these approaches frequently entail intricate processing steps, high-temperature requirements, or substantial financial investments, thereby limiting their scalability and practical applicability for large-scale energy storage systems. The integration of a conductive interfacial buffer layer is a well-established and effective strategy in solid-state LIBs and SIBs, known to significantly improve interfacial contact, reduce impedance, and enhance overall electrochemical performance.[25,26] A widely used approach to enhance interfacial contact in SSIBs involves introducing a small amount of OLE at the electrode–SE interface.[27] While this method may initially reduce interfacial resistance, it often leads to poor long-term stability due to the formation of resistive decomposition byproducts.[20] Ionic liquids have also been explored as interfacial modifiers and have shown significant improvements in both discharge capacity and cycling stability.[28] Nonetheless, their high cost, limited air stability, and processing complexity hinder widespread adoption.[29] Composite polymer electrolytes (CPEs), incorporating both polymer and ceramic phases, have gained attention as promising alternatives due to their ability to form conformal interfaces and reduce

interfacial resistance.[30,31] While they demonstrate enhanced electrochemical performance, these systems often suffer from limited electrochemical stability windows, and frequently required elevated temperatures for adequate ionic conduction, thus limiting their applicability at room temperature. To address these challenges, Wang et al.[32] introduced an asymmetric SE design that combines the merits of polymer and ceramic electrolytes. In their study, a polyethylene oxide (PEO)-succinonitrile-$NaClO_4$ based polymer layer was applied selectively at the sodium anode-ceramic electrolyte interface. This strategy delivered an impressive capacity retention of 99.6% over 100 cycles at 50 °C temperature. Similarly, Shindrov et al.[33] fabricated solid-state cells using a PEO-$NaClO_4$-NZSP composite electrolyte, achieving a specific capacity of 60 mAh g^{-1} at 60 °C. In our previous work, we adopted an interfacial engineering approach to design an SSIB by incorporating PEO-NZSP-$NaClO_4$-based composite electrolyte between the cathode and SE, while using Na metal as the anode.[34] Although the introduction of a polymer layer as an interface modifier has been a promising route, designing an all-solid-state full cell using this approach has seldom been reported. This polymer-integration strategy at the interface simultaneously mitigates the mechanical mismatch and chemical instability at the solid–solid interface, offering a scalable route to construct thermally robust and ionically conductive interfaces in SSIBs.

Building upon recent advances in interfacial engineering, the present study introduces a novel design for an all-solid-state symmetric SIB that prioritizes enhanced safety, cost-effectiveness, and practical scalability. A key innovation lies in the integration of a conductive polymer-based interfacial layer (CBPL) at the ceramic SE-electrode interface. The ionic conductivity of the CBPL is systematically optimized by varying the salt concentration and active filler content. Importantly, the CBPL layer demonstrates excellent environmental stability, enabling cell assembly under ambient conditions and eliminating the need for inert-atmosphere processing—an advancement that significantly lowers fabrication complexity and cost. This interfacial engineering strategy resulted in a pronounced enhancement in electrochemical stability, with the symmetric SSIB retaining 89% of its capacity over extended galvanostatic charge–discharge (GCD) cycling. Postcycling analysis revealed that CPBL not only improved ionic transport but also served as an effective protective barrier, mitigating active material (AM) degradation during operation. This work demonstrates, for the first time, a robust and scalable approach to realizing high-performance, durable, and safe symmetric SSIBs operable under ambient conditions—establishing a new direction for practical solid-state SIB technologies.

2. Experimental Section

2.1. Materials

Na_2CO_3 (≥99.5%), NH_4VO_3 (≥99%), $C_6H_8O_7$ (≥99.5%), $Fe(NO_3)_3\cdot9H_2O$ (≥99.5%), $NH_4H_2PO_4$ (≥98%), and SiO_2 (99.5%)

Batteries & Supercaps

Research Article
doi.org/10.1002/batt.202500372

Chemistry Europe
European Chemical
Societies Publishing

were purchased from Alfa Aesar (UK). MgO (99%), propylene carbonate (99.7%), $NaClO_4$ ($\geq$98%), and polyvinylidene fluoride (PVDF) were obtained from Sigma–Aldrich (USA). Poly(ethylene oxide) with a molecular weight of 10^6 g mol^{-1}, N-methyl-2-pyrrolidone (NMP), and ethanol were sourced from Merck Chemicals (Germany). Single-walled carbon nanotubes (SWCNTs) were acquired from Techinstro (India). ZrO_2 (99.9%) and acetonitrile (ACN, 99.5%) were obtained from Tosho Corporation (Japan) and Loba Chemicals (India), respectively. All chemicals were used as-received, without further purification, for the fabrication of electrodes, SEs, and polymer composite films.

2.2. Characterization

2.2.1. Structural Characterization

Phase analysis was conducted using X-ray diffraction (XRD) on a PANalytical X'Pert Powder diffractometer (Netherlands), with data collected over a 2θ range of 10–70° at a step size of 0.01°, employing Cu Kα as the incident radiation. The microstructure of the pristine and cycled electrodes, as well as the CPBL films, was examined using field-emission scanning electron microscopy (FE-SEM, FEI Nova NanoSem-450) at an acceleration voltage of 15 kV. Fourier-transform infrared (FTIR) spectroscopy was carried out using a Bruker Tensor 27 spectrometer (Germany) to identify functional groups present in the CPBL, pristine and cycled electrodes. Spectra were recorded over a wavenumber range of 400–4000 cm^{-1}. The X-ray photoelectron spectroscopy (XPS) data were recorded using a K-alpha X-ray photoelectron spectrometer equipped with Al-Kα microfocused monochromator (Thermo Fisher Scientific Inc. Waltham, USA).

2.2.2. Electrochemical Characterization

Electrochemical characterization of the symmetric SSIBs was conducted at RT using CR2032 coin cells on an Arbin 232,255 battery testing system (USA). Electrochemical impedance spectra (EIS) were acquired using a Gamry 1010E potentiostat (USA), with measurements recorded at an amplitude of 50 mV over a frequency range of 1 MHz to 0.1 Hz at RT. Ionic conductivity was determined by analyzing the impedance spectra obtained from Au-electroded CPBL films over a temperature range of RT to 50 °C, using a Solartron 1260A impedance analyzer (UK). Impedance data were recorded using Z-plot software (Scribner Associates Inc., USA) across a frequency range of 10 MHz to 1 Hz, with an applied potential amplitude of 50 mV. Cyclic voltammetry (CV) was carried out over a potential window of 1–2.5 V at scan rates of 0.01, 0.03, 0.05, 0.08, and 0.1 mV s^{-1}. GCD measurements were conducted between 1 and 2.5 V at RT, with current rates ranging from C/8 to 1C. The charge/discharge current was calculated based on the theoretical capacity of the anode ($\approx$58.8 mAh g^{-1}), as both the anode and cathode were used in equal weight ratios (1:1) in the symmetric cell configuration.

2.3. Full Cell Fabrication

2.3.1. Synthesis of Mg-Doped NZSP Ceramic Electrolyte

The synthesis of Mg-doped NZSP (NMZSP) was carried out using a conventional solid-state reaction route, as outlined in our previous studies.[19] A polycrystalline powder with the nominal composition $Na_{3.456}Mg_{0.128}Zr_{1.872}Si_{2.2}P_{0.8}O_{12}$ was initially prepared by mixing stoichiometric quantities of high-purity precursor materials. The constituents were blended in ethanol to form a slurry using a planetary ball mill for 4 h, followed by drying in an oven at 80 °C overnight. The dried powder was then calcined at 1000 °C for 5 h, ground, and subjected to a second calcination under similar conditions to ensure compositional uniformity. Postcalcination, the powder was again ball-milled in ethanol for another 4 h and dried overnight to achieve a fine particle size. Subsequently, 0.2 wt.% polyvinyl alcohol (PVA) binder was added to the dried powder, along with acetone, and the mixture was homogenized using an agate mortar and pestle. The resulting binder-mixed powder was pressed into disk-shaped pellets (10 mm diameter, $\approx$1.5 mm thickness) via uniaxial compaction, followed by cold isostatic pressing at 300 MPa for 5 min to enhance density uniformity. Final sintering was conducted in ambient air at 1250 °C for 5 h, with an intermediate dwell at 615 °C for 2 h to facilitate binder burnout. To prevent cracking during sintering, a sacrificial pellet of identical composition was placed beneath the actual sample. A few sintered NMZSP pellets were subsequently ground using an agate mortar and pestle, sieved, and employed as ceramic fillers in the fabrication of CPBL.

2.3.2. Fabrication of CPBL

Self-standing composite polymer films were fabricated via a conventional solution casting approach for electrical conductivity measurement. PEO powder was initially dispersed in ACN, resulting in a homogeneous and transparent viscous solution. $NaClO_4$ salt was then added in varying amounts corresponding to specific ethylene oxide to sodium (EO:Na) molar ratios, along with 6 μL of propylene carbonate (PC) as a plasticizer. The resulting mixture was magnetically stirred at RT for 6 h to ensure thorough uniformity. Subsequently, ground NMZSP powder was introduced into the PEO solution at varying loadings (5, 10, 15, and 20 wt.%), followed by an additional 6 h of continuous stirring to achieve a well-dispersed composite solution.

The obtained viscous mixtures were cast onto clean glass Petri dishes and subjected to vacuum drying at 35 °C for 8 h to ensure complete removal of residual ACN, leading to the formation of uniform self-standing films. The final films exhibited a consistent thickness in the range of 120–130 μm. For electrochemical characterization, circular disks with a diameter of 12 mm were punched from the dried films. The optimized CPBL composition was subsequently employed to modify the interface between the electrode and the SE, aiming to enhance interfacial stability and overall cell performance.
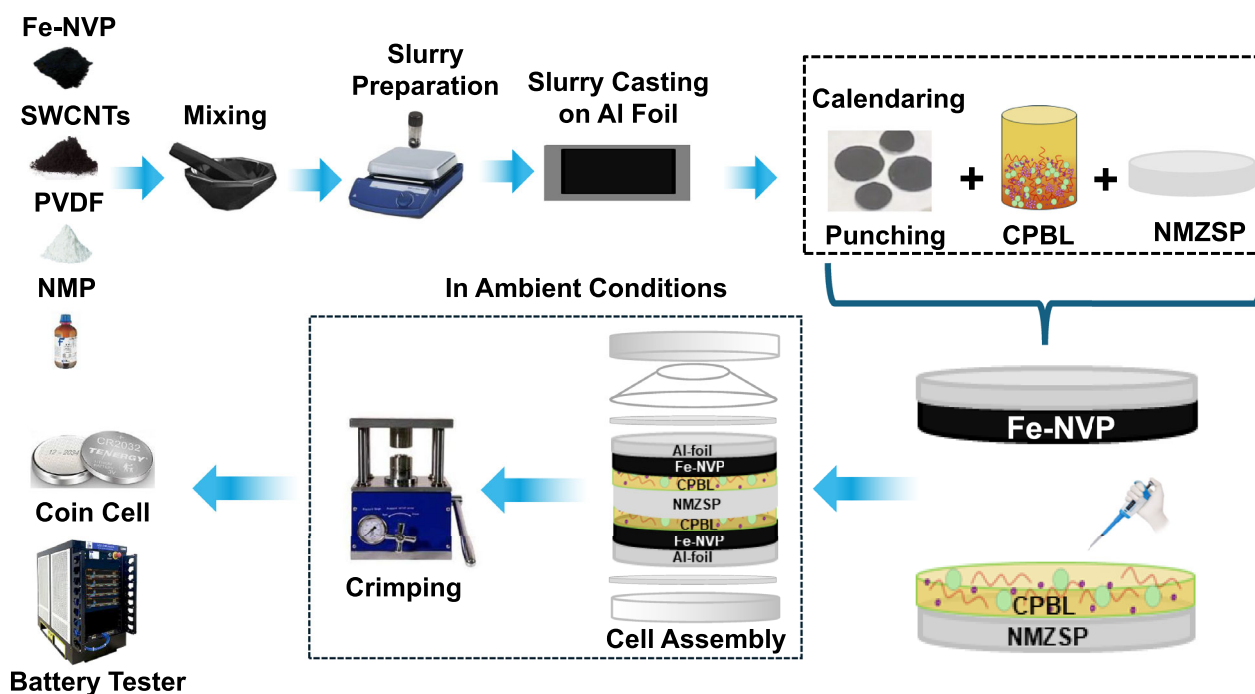
Batteries & Supercaps

Research Article
doi.org/10.1002/batt.202500372

Chemistry Europe
European Chemical
Societies Publishing

Figure 1. Schematic illustration of the steps involved in electrode preparation and symmetric SSIB fabrication.

2.3.3. Electrode Preparation

The electrode of the symmetrical SSIBs was prepared by combining hydrothermally synthesized $Na_3V_{1.85}Fe_{0.15}P_3O_{12}$ (Fe-NVP) powder (AM) with SWCNTs as the conductive additive and PVDF as the binder in a fixed weight ratio of 75:15:10. The synthesis details of Fe-NVP powder are provided elsewhere.[35] **Figure 1** shows the steps involved in the electrode fabrication. The mixture was initially manually homogenized in an agate mortar for 1 h to ensure uniform distribution of all components. Subsequently, the resulting powder mixture was dispersed in NMP and stirred continuously for 24 h to obtain a uniform electrode slurry. This slurry was evenly cast onto aluminum foil (serving as the current collector) using the doctor blade technique. The coated electrodes were then dried in a vacuum oven at 90 °C overnight to ensure complete removal of residual solvent. After drying, the electrodes were calendared and punched into 8 mm diameter discs, yielding an AM loading of 0.59 mg cm^{-2}, for subsequent characterization and electrochemical evaluation.

2.3.4. Symmetric Cell Fabrication

A key advantage of the studied SSIB full cell lies in its ability to assemble under ambient conditions, outside of an inert gas-filled glove box. The full cells, denoted as Fe-NVP | CPBL-NMZSP-CPBL | Fe-NVP, were constructed using Fe-NVP as the AM for both the cathode and anode, NMZSP as the SE, and a CPBL at both the cathode–SE and anode–SE interfaces to enhance interfacial stability. The cathode, anode, and SE were fabricated, following the procedures outlined in the preceding section. For improved interfacial contact, 15 µL of CPBL was applied to the surfaces of both the anode and cathode to fabricate a symmetric SSIB stack (cathode–SE-anode), which was then left to age for 24 h prior to cell assembly. The SSIB stack was crimped in a CR2032 coin cell holder under ambient conditions at 30 °C, as depicted in the schematic in Figure 1.

3. Results and Discussion

3.1. Composition Optimization of CPBL

Figure 2 illustrates the structural characterization of the as-fabricated CPBL film. As a first step, XRD analysis was conducted on the CPBL film with the optimized composition, as presented in Figure 2a. The resulting XRD pattern reveals distinct diffraction peaks attributable to both the NMZSP filler and the PEO polymer matrix. The concurrent presence of these characteristic peaks confirms the effective incorporation of the ceramic filler within the polymer host and highlights the excellent structural compatibility and phase stability between NMZSP and PEO.

Figure 2b presents the FTIR spectra of both pure PEO and CPBL films, recorded over the range of 500–4000 cm^{-1}, to analyze their molecular structure and chemical interactions. The presence of $NaClO_4$ in its dissociated form within the CPBL matrix is confirmed by the characteristic peak for the $(ClO_4)^-$ at 625 cm^{-1}. The peaks located at 1184 and 1791 cm^{-1} are attributed to the incorporation of PC plasticizer. In particular, the peak identified at 1791 cm^{-1} corresponds to the stretching vibration of the carbonyl (C=O) bond in PC, verifying its successful integration
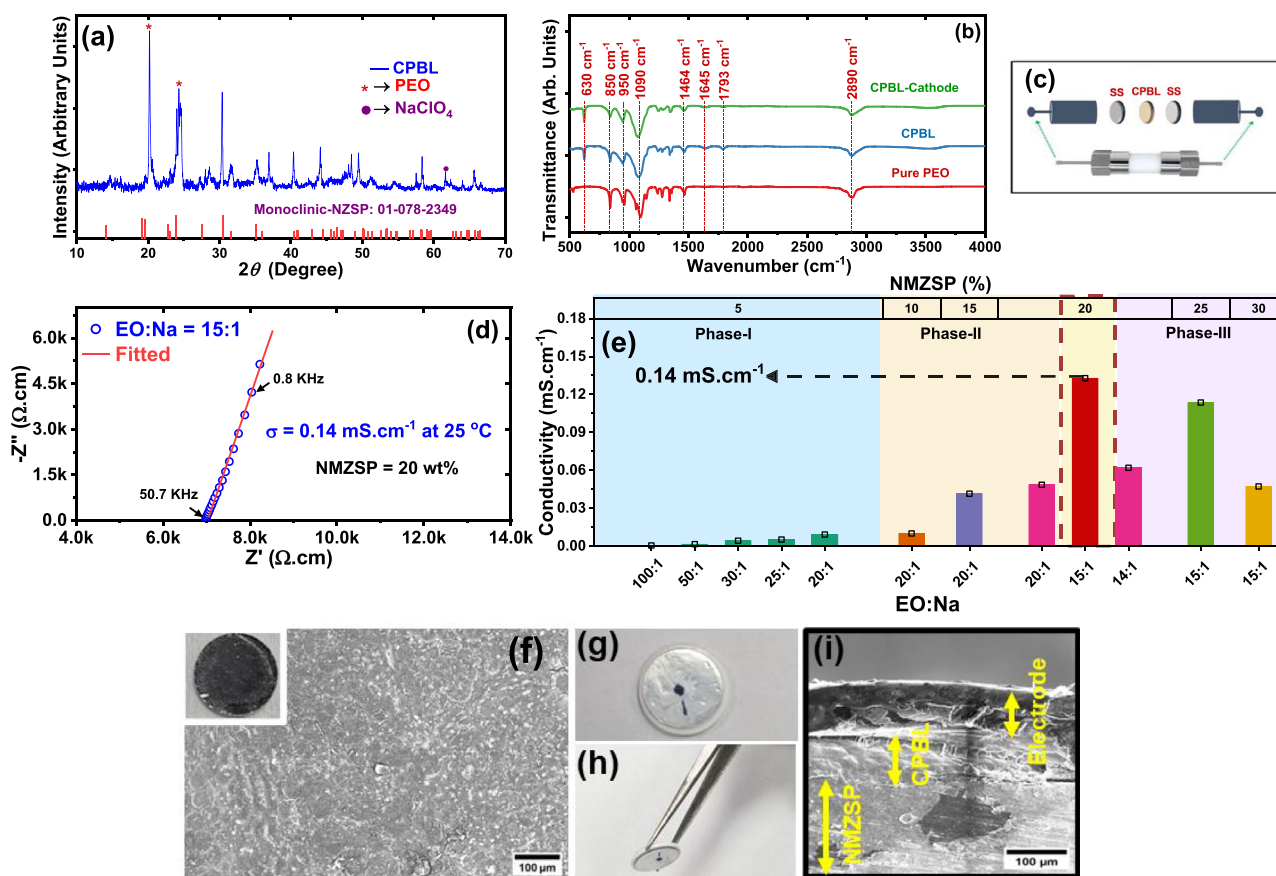
Figure 2. a) XRD pattern of the CPBL film; b) FTIR spectra of PEO, CPBL, and the CPBL-coated electrode; c) schematic of the Swagelok-type cell used for conductivity measurement of the CPBL film; d) EIS spectrum of the SS|CPBL|SS assembly with an EO:Na ratio of 15:1 and NMZSP content of 20 wt.%; e) bar plot showing conductivity evolution for various composite compositions; f) FE-SEM and optical (inset) image of the CPBL-coated electrode; g,h) top and side views of the SSIB cell; and i) FE-SEM image of the cross-section of the SSIB cell.

into the polymer network. The inclusion of PC not only modifies the polymer environment but also plays a critical role in enhancing the ionic conductivity of the CPBL film by promoting greater polymer chain flexibility and increasing the concentration of free mobile ions. Furthermore, the broad hump observed at $3550\,cm^{-1}$ and the distinct peak at $1634\,cm^{-1}$ are assigned to the stretching and bending vibrations of the O—H group, respectively.[36,37] Figure 2c shows the schematic of a Swagelok-type cell used for the conductivity measurement of the CPBL film.

Figure 2d presents the Nyquist plot of the CPBL film with an EO:Na molar ratio of 15:1, measured using a Swagelok cell. The impedance spectrum exhibits a notably low bulk resistance and shows no semicircle feature, indicating efficient ionic transport within the polymer electrolyte. This low resistance directly correlates with a high ionic conductivity, which is calculated as $1.4 \times 10^{-1}\,mS\,cm^{-1}$ at ambient temperature. Such enhanced conductivity is critical for the practical application of CPBL films in SSIBs, as it ensures minimal interfacial resistance and improved electrochemical performance. Figure 2e illustrates the dependance of ionic conductivity on both the salt concentration and active ceramic filler content in the CPBL film. The bar plot highlights the combined effects of the NMZSP filler and sodium salt

(NaClO$_4$) on the conductivity performance of the CPBL film. Salt concentration is represented by the ethylene oxide to sodium ion (EO:Na) molar ratio, while the active filler content is expressed in wt.%. The chemical composition optimization of the composite polymer film to achieve high ionic conductivity was carried out in three systematic phases. In the first phase, the salt concentration was varied while maintaining the active filler content at 5 wt.%. A gradual increase in ionic conductivity was observed with increasing NaClO$_4$ concentration, reaching a maximum at an EO:Na molar ratio of 20:1. In the second phase, the EO:Na ratio was held fixed at 20:1, and the NMZSP filler content was incrementally increased up to 20 wt.% to evaluate its effect on conductivity. This step helped identify the optimum filler loading required to facilitate ion transport without impeding polymer chain mobility. In the final phase, the salt concentration was further increased by reducing the EO:Na ratio to 15:1, which resulted in the highest recorded ionic conductivity for the system. However, a further reduction in the EO:Na ratio led to a decline in conductivity. Similarly, increasing the active filler content at this higher salt concentration also decreases ionic conductivity, indicating the importance of balancing salt and filler levels to avoid excessive structural rigidity or ion aggregation.[38,39]

Batteries & Supercaps

Research Article
doi.org/10.1002/batt.202500372

Chemistry Europe
European Chemical
Societies Publishing

The results demonstrate that the ionic conductivity of the composite system is governed by a delicate interplay between the degree of salt dissociation and the extent of filler–polymer interaction, both of which influence ion mobility and the structural dynamics of the polymer matrix.

Figure 2f presents the FE-SEM image of the CPBL-coated electrode, with the corresponding optical micrograph shown in the inset. The image reveals that the CPBL covers the entire electrode area without forming pores and macrocracks. The NMZSP filler is homogeneously distributed, suggesting a uniform morphology achieved during fabrication. Figure 2g,h present optical images of the top and side views of the assembled symmetrical cell, respectively. The images reveal that the electrode layer is uniformly and firmly attached to the SE. Figure 2i presents the cross-sectional FE-SEM image of the SSIB, where the distinct layers of the NMZSP pellet, CPBL, and the electrode are visible. The CPBL exhibits a uniform distribution with a thickness of ≈80–90 μm. The electrode-SE adhesion is facilitated by the presence of the CPBL, which acts as a compliant interfacial medium that accommodates surface roughness and fills interfacial voids. The CPBL promotes interfacial integration, which is essential for maintaining low interfacial resistance and stable electrochemical performance.

3.2. Electrochemical Characterization of SSIBs

This section presents the electrochemical performance of symmetric SSIBs using Fe-NVP as electrodes. The theoretical capacity of NVP, when employed as a cathode, is 117.6 mAh g^{-1}, corresponding to the full utilization of the V^{3+}/V^{4+} redox couple.

In the Fe-NVP structure, iron partially substitutes electrochemically active vanadium within the crystal lattice. However, Fe remains electrochemically inactive during cycling, and the redox activity is solely attributed to the V^{3+}/V^{4+} occurring in the remaining V. Consequently, the number of electrons involved per formula unit is reduced to ≈1.85 mol, thereby lowering the theoretical capacity of Fe-NVP to ≈109 mAh g^{-1} when used as a cathode.[35]

Conversely, when Fe-NVP functions as an anode, the redox activity is limited to the V^{2+}/V^{3+} couple, involving a single-electron transfer per formula unit. This results in a theoretical capacity of ≈58.7 mAh g^{-1}. In this study, equal mass loadings of Fe-NVP were used for both electrodes; thus, the overall cell capacity is constrained by the lower theoretical capacity of the anode.

Figure 3 presents the electrochemical performance analysis of the symmetrical SSIB operating at RT. The cell is assembled entirely under ambient conditions, without the use of an inert gas-filled glove box, thereby demonstrating the excellent air stability of the constituent materials. In this configuration, Fe-NVP serves as AM for both cathode and anode, while NMZSP functioned as the SE. A CPBL film is incorporated as a protective buffer layer, ensuring enhanced interfacial contact and stability and facilitating efficient sodium-ion transport across the electrode-SE interfaces.

EIS is measured on the as-assembled symmetric SSIB, both before and after cycling, as shown in Figure 3a. The Nyquist plot reveals a depressed semicircle in the high-frequency region, corresponding to the charge transfer resistance (R_{ct}), followed by a linear tail in the low-frequency region, which is characteristic of Warburg impedance associated with ion diffusion. The impedance spectra taken on symmetric SSIB before and after cycling
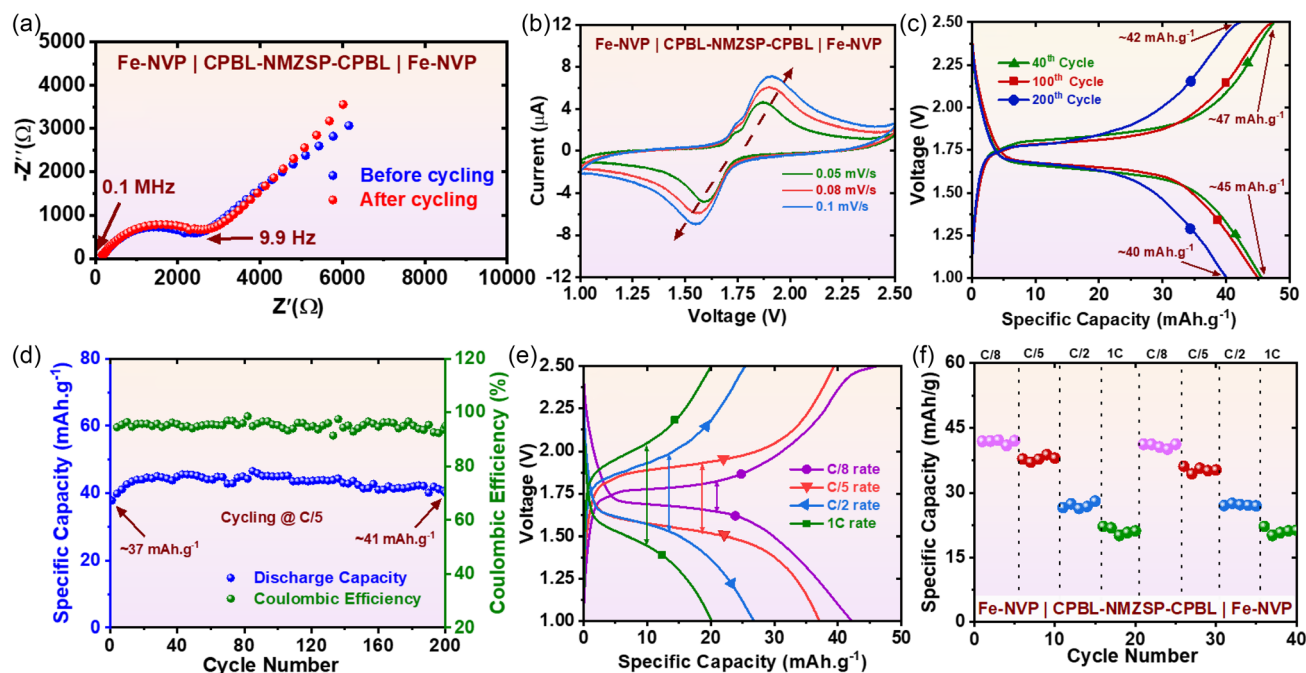

Figure 3. Electrochemical performance of the symmetric SSIB: a) EIS of the full cell before and after cycling; b) CV at various scan rates; c) GCD profiles at the 40th, 100th, and 200th cycles at a C/5 rate; d) cycling performance at a C/5 rate; e) GCD profiles at different C-rates; and f) rate capability analysis.

Batteries & Supercaps

Research Article
doi.org/10.1002/batt.202500372

Chemistry
Europe

European Chemical
Societies Publishing

reveal an increase in R_{ct} value from ≈3000 to ≈3500 Ω. This rise in R_{ct} value is indicative of interfacial degradation, attributable to partial deterioration of the CPBL layer during repeated GCD cycling, as confirmed by postcycling analysis presented in a subsequent section. CV profiles are recorded at scan rates of 0.05, 0.08, and 0.1 mV s^{-1} to analyze the redox reaction peak positions and assess the reversibility of the Fe-NVP electrode reactions, as shown in Figure 3b. The oxidation peaks are observed at around 1.87, 1.90, and 1.92 V, while the corresponding reduction peaks appear at 1.59, 1.56, and 1.54 V, for the respective scan rates. As the scan rate increases, the potential gap between oxidation and reduction peaks widens, indicating enhanced polarization. This growing separation reflects a deviation from a fully reversible redox process at lower scan rates toward quasireversible or partially irreversible behavior at higher scan rates.

Figure 3c illustrates the GCD profiles of the symmetrical SSIB cycled at a C/5 rate, comparing the 40th, 100th, and 200th cycles to assess the long-term electrochemical stability of the cell. As cycling progresses, the discharge capacity gradually declines, while the voltage gap between the charge and discharge plateaus remains largely unchanged. The specific capacities at the 40th, 100th, and 200th cycles are ≈46, 44, and 41 mAh g^{-1}, respectively, indicating progressive capacity fade over extended cycling, likely due to AM degradation or loss. Figure 3d shows the cyclability performance of the symmetric SSIB at a C/5 rate over 200 cycles. Initially, the cell displays an increase in discharge capacity from ≈37 to 45 mAh g^{-1} within the first few cycles, after which it stabilizes. The capacity remains steady up to around 150 cycles, with only minor fluctuations. Beyond this point, the capacity gradually declines to ≈41 mAh g^{-1} at the 200th cycle, corresponding to about 91% retention of the stabilized capacity.

Figure 3f presents the rate-capability analysis of the cell after long-term cycling at a C/5 rate, evaluated at various C-rates (C/8, C/5, C/2, and 1C) by cycling for five cycles at each rate. This assessment determines the cell capacity retention under increasing current densities, transitioning from low to high C-rates. Subsequently, the cell is recycled starting again from the initial low C-rate of C/8 up to 1C, to examine the recoverability of specific capacity. The cell delivers discharge capacities of ≈42, 39, 28, and 22 mAh g^{-1} at C/8, C/5, C/2, and 1C, respectively. Upon returning to the initial C/8 rate and ramping back up to 1C, the cell demonstrates excellent capacity recovery, retaining around 98% of the initial discharge capacity at each corresponding C-rate.

Figure 3e displays the voltage gap between the charge–discharge plateaus, measured at C/8, C/5, C/2, and 1C rates over three cycles at approximately half the cell's capacity, evaluating the reversibility of the electrochemical reactions under varying current densities. As the C-rate increases from C/8 to 1C, a corresponding rise in the potential difference between the charge and discharge plateaus is observed. The voltage gaps are ≈0.18, 0.41, 0.46, and 0.60 V at C/8, C/5, C/2, and 1C, respectively. This increasing trend reflects higher polarization at elevated current densities, indicating a decline in reaction reversibility as the cell operates at faster charge/discharge rates.

Till now, very few studies have reported on symmetrical SSIB cells using NVP-based electrodes and ceramic SE. **Table 1** summarizes these reports, comparing the electrochemical performance of various symmetrical SSIBs. It is noteworthy that a cathode-to-anode AM weight ratio of 1:2 in an NVP-based symmetric cell corresponds to a theoretical capacity of ≈117.6 mAh g^{-1}, while a 1:1 ratio yields ≈58.8 mAh g^{-1}. These differences are critical for interpreting rate performance and capacity retention across studies.

In a recent study, Dwivedi et al.[22] designed a symmetrical SSIB comprising a composite electrolyte of PEO-sodium bis(trifluoromethylsulfonyl)imide (NaTFSI) and Na$_{3.3}$Zr$_{1.8}$Mg$_{0.1}$Sc$_{0.1}$Si$_2$PO$_{12}$ (NZSP-0.1 MS), and Zn-doped NVP-based composite electrodes incorporating NZSP-0.1 MS, PVDF-NaTFSI, and conducting carbon additives. Cycling at C/2 resulted in about 80 mAh g^{-1} initial capacity, with capacity retention of 85% after 80 cycles at 60 °C. Similarly, Wang et al.[31] reported the fabrication of an NVP//NVP symmetric

Table 1. Comparison of performance metrics achieved from various symmetrical SSIBs reported in the literature. (Full form for the various abbreviations used in the table is given as: NYSO: Na$_5$YSi$_4$O$_{12}$; NVPOF: Na$_3$V$_2$(PO$_4$)$_2$O$_2$F; C$_{sp}$: carbon super P; NaTFSI: sodium bis(trifluoromethylsulfonyl)imide; NVZP: Zn-doped NVP; NZSP-0.1 MS: Na$_{3.3}$Zr$_{1.8}$Mg$_{0.1}$Sc$_{0.1}$Si$_2$PO$_{12}$; NZSP-25 wt.% PEO: composite SE of NZSP and PEO.

Anode	Cathode	SE	Full cell configuration	Initial capacity [mAh g^{-1}]	Electrochemical performance (%Capacity retention after n cycles @ C-rate)	Reference
Calculation of current rate based on cathode theoretical capacity						
NVP	NVPOF	NYSO	NVPOF//NYSO//NVP	82 @ 1C	74% after 50 cycles 1C	[47]
NVP	NVP	NZSP	NVP//NZSP//NVP	68 @ 1.2 μAcm^{-2},	NA	[24]
NVP-NZSP-C$_{sp}$ (25:60:15)	NVP-NZSP-C$_{sp}$ (25:60:15)	NZSP	NVP//NZSP//NVP	1.04 mAh cm^{-2} @ C/10-200 °C	NA	[21]
NVZP	NVZP	PEO–NaTFSI/ NZSP-0.1MS	NVZP//PEO-NaTFSI-NZSP-0.1MS//NVZP	≈80@ C/2-60 °C	85% after 80 cycles @C/2	[22]
NVP	NVP	ferro-NaClO$_4$/ PEO-NZSP	NVP//ferro-NaClO$_4$-PEO-NZSP//NVP	≈72@C/2	86.4% after 650 cycles @C/2	[31]
Calculation of the current rate based on the anode theoretical capacity						
NVP	NVP	NZSP-25 wt.% PEO	NVP//NZSP-25 wt.% PEO//NVP	41.2 @ C/10	83.7% after 100 cycles @ 0.1C	[30]
Fe-NVP	Fe-NVP	NMZSP	Fe-NVP // CPBL-NMZSP - CPBL // Fe-NVP	45 mAh g^{-1}@ C/5	89% retention after 200 cycles	Present work

Batteries & Supercaps

Research Article
doi.org/10.1002/batt.202500372

Chemistry Europe
European Chemical
Societies Publishing

cell employing a composite SE composed of NZSP—PEO—NaClO$_4$, with the electrode-SE interface engineered using a ferroelectric K$_{0.5}$Na$_{0.5}$NbO$_3$ coating. The resulting SSIB demonstrated outstanding cycling stability, retaining 86.4% of its capacity after 650 cycles at a C/2 rate. In another investigation, Wang et al.[30] developed a symmetric NVP-based SSIB employing a PEO-NATFSI-NZSP composite electrolyte. The inherent flexibility of the composite SE enabled intimate and stable contact with ceramic electrodes at RT, resulting in low interfacial impedance and enhanced durability. The cell delivered an initial discharge capacity of 41.2 mAh g^{-1} at C/10 and retained 83.7% of its capacity after 100 cycles, considering a theoretical capacity of ≈55 mAh/g based on the anode. The symmetric cell fabricated in the present study employed Fe-doped NVP as the

AM for both electrodes in equal proportions, NMZSP as the SE, and a CPBL as the interface modifier. This configuration delivered an initial discharge capacity of ≈45 mAh g^{-1} and demonstrated 89% capacity retention over 200 cycles at a C/5 rate. These electrochemical performance metrics are comparable to previously reported values and underscore the effectiveness of CPBL-based interface modification in advancing the commercial viability of symmetric SSIBs.

3.3. Postcycling Characterization of Symmetric SSIBs

Following electrochemical performance evaluation, a CV analysis is conducted at a lower scan rate of 0.03 mV s^{-1}, as shown in **Figure** 4a. The well-defined oxidation and reduction peaks
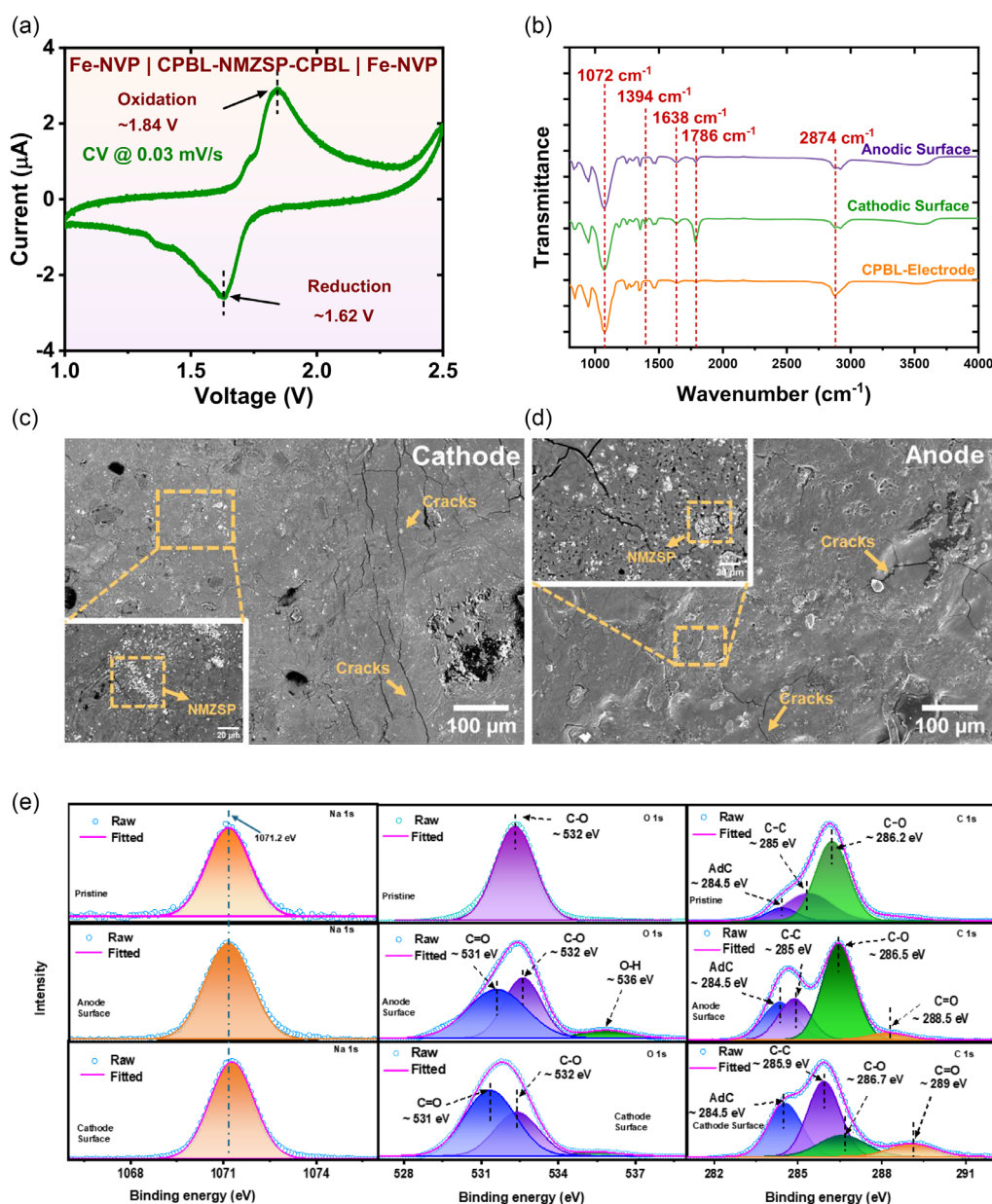

Figure 4. Postcycling characterization of the symmetric full cell: a) CV; b) FTIR spectra of pristine and cycled electrodes; c,d) FESEM images of the cathodic and anodic surfaces; and e) XPS of pristine and cycled electrodes.

appear at approximately 1.84 and 1.62 V, respectively, confirming that the electrode material remains electrochemically active after prolonged cycling. The sharp and distinct nature of these peaks indicates efficient charge transfer kinetics and suggests that the electrode–SE interface retains excellent structural and electrochemical stability.

To elucidate the role of the buffer layer and gain a deeper understanding of the interfacial changes during cycling, a postmortem analysis of the cycled cell was performed using FTIR, SEM, and XPS on both electrodes (as shown in Figure 4b,c,d,e). The cycled cell was disassembled, and detailed characterizations were carried out on both the anode and cathode of the SSIB. SEM images in Figure 4c,d reveal the formation of cracks and pores on the anodic and cathodic surfaces, along with a slight segregation of NMZSP filler, as shown in the insets. These mechanical features result from the repeated insertion and extraction of sodium ions. However, the deformations are confined to small areas, while the polymer buffer layer remains uniformly intact across the electrode surface. This finding suggests that CPBL degradation is limited and localized, rather than widespread, highlighting its structural resilience during cycling.

The chemical alterations at the electrode-SE interfaces were investigated using FTIR and XPS characterization (shown in Figure 4b,e, respectively). Figure 4b shows a moderate enhancement in the intensity of the 1786 cm^{-1} band on both the postcycled cathodic and anodic surfaces, indicating an increase in carbonyl, ester, or carbonate-type compounds. This enhancement likely arises from oxidative degradation of the PEO matrix during electrochemical cycling, as reported in previous studies.[40,41] Notably, the 1786 cm^{-1} band is significantly more intense on the cathodic surface than on the anodic side, suggesting that oxidative degradation is more prominent at the cathode-SE interface. Deconvolution of C 1s and O 1s core XPS spectra further confirms the presence of carbonyl-type species on both electrodes after cycling, with characteristic peaks at ≈289 eV (C 1s) and ≈531 eV (O 1s).[41,42] The intensity of these XPS peaks is also higher on the cathodic surface compared to the anodic surface, further corroborating the earlier observation that oxidative degradation is more pronounced on the cathode side. The peaks observed at ≈286 eV in C 1s spectrum and ≈532 eV in O 1s spectrum, corresponding to C—O bonds, exhibit a more pronounced reduction on the cathodic surface after cycling. This suggests the dissociation of C—O bonds, leading to the formation of carbonyl-type degradation products.[42] The peak observed at 284.5 eV in the C 1s spectra corresponds to adventitious carbon (AdC), which likely appeared due to prolonged air exposure before XPS characterization.[43]

Moreover, the emergence of broad bands near 3500 and 1638 cm^{-1} in the FTIR spectra of both electrodes after cycling indicates that the decomposition of CBPL also resulted in the formation of hydroxyl-type compounds.[36,37] The deconvoluted O 1s spectrum of the anodic surface further confirms the presence of —OH type compounds, as evidenced by the distinct peak observed at 536 eV.[42] Furthermore, the splitting of the CH$_2$ stretching band at ≈2866 cm^{-1} in the postcycled FTIR spectra, suggests the presence of both symmetric and asymmetric C—H stretching vibrations.[44] This can be attributed to the occurrence of salt polymer decoupling or the polymer chain scission,[45] which leads to a change in the chemical environment of —CH$_2$. Apart from the observed changes, no additional peaks indicative of significant CPBL degradation were detected.

In Figure 4b a prominent band is observed near 1072 cm^{-1} across all samples, corresponding to the C—O—C bond, which is a characteristic of PEO backbone.[46] The unalteration of this band after cycling suggests that the CPBL layer remains structurally intact, despite the occurrence of oxidative side reactions. This stability is further supported by the Na 1s XPS spectra, which shows no significant shift postcycling, indicating minimal disruption in the chemical environment of sodium ions within the polymer matrix.

Thus, the combined XPS and FTIR analysis, along with the microstructural observations, support the hypothesis that while interfacial degradation is more pronounced at the cathode side, it remains spatially confined, likely limited to the surface region. This localized degradation appears insufficient to significantly hinder charge transfer. The structural integrity and mechanical flexibility of the CPBL layer likely play a pivotal role in maintaining interfacial contact and preventing delamination, thereby preserving continuous ion conduction. Consequently, the SSIB retains stable electrochemical performance, underscoring the critical function of the CPBL in mitigating interfacial degradation and enhancing long-term cell stability.

4. Conclusion

This study presents the first successful integration of a composite polymer buffer layer in a symmetric SSIB with a NASICON-type ceramic electrolyte, demonstrating its critical role in overcoming interfacial limitations. The CPBL, synthesized via a solution-casting method using a PEO-based composite with NaClO$_4$ salt, propylene carbonate as a plasticizer, and NMZSP as an active filler, exhibited a high RT ionic conductivity of 0.14 mS cm^{-1}. When applied between Fe-doped NVP electrodes and the NMZSP solid electrolyte, the CPBL enabled intimate and stable interfacial contact, leading to outstanding electrochemical performance. The resulting symmetric SSIB delivered an initial discharge capacity of ≈45 mAh g^{-1} at C/5 and retained 89% of its capacity over 200 cycles, approaching the theoretical capacity of Fe-NVP (≈58.8 mAh g^{-1}). Postcycling characterization of the cell revealed localized degradation of the CPBL confined to the electrode surface, with no significant structural breakdown in the bulk. The inherent structural flexibility of the CPBL facilitated intimate and stable interfacial contact, ensuring continuous ionic conduction throughout extended cycling. These results underscore the effectiveness of CPBL in enhancing interfacial stability and cycling durability without the need for complex processing conditions, establishing a promising pathway for the scalable development of safe, efficient, and sustainable solid-state sodium-ion energy storage systems.

Batteries & Supercaps

Research Article
doi.org/10.1002/batt.202500372

Chemistry Europe
European Chemical
Societies Publishing

Conflict of Interest

The authors declare no conflict of interest.

Author Contributions

Saurabh Sharma: investigation; methodology; data curation; formal analysis; visualization; writing—original draft. **Sandipan Bhattacharyya**: investigation; data curation; visualization; formal analysis; writing reviewing & editing. **Ravi P. Srivastava**: investigation; formal analysis; visualization; writing reviewing & editing. **Sourabh Shyamal**: data curation; formal analysis; reviewing & editing. **Mohd Aman**: data curation; visualization; reviewing & editing. **Shobit Omar**: conceptualization; investigation; visualization; supervision; writing reviewing & editing; funding acquisition.

Data Availability Statement

The data that support the findings of this study are available from the corresponding author upon reasonable request.

[1] D. Larcher, J. M. Tarascon, *Nat. Chem.* **2015**, *7*, 19.
[2] M. Aman, P. Konduparty, S. Sharma, R. P. Srivastava, S. Bhattacharyya, V. Sharma, K. Balani, S. K. Jha, S. Omar, *J. Energy Storage* **2025**, *116*, 116093.
[3] K. Singh, A. Chakraborty, R. Thirupathi, S. Omar, *Ionics* **2022**, *28*, 5289.
[4] K. Yanamandra, D. Pinisetty, N. Gupta, *Renewable Sustainable Energy Rev.* **2023**, *173*, 113078.
[5] P. Phogat, S. Rawat, S. Dey, M. Wan, *J. Alloys Compd.* **2025**, *1020*, 179544.
[6] G. Li, H. Ma, Y. Tong, H. Wang, Y. Luo, E. H. Ang, S. Bohm, A. A. Ibrahim, A. Umar, *J. Energy Storage* **2025**, *107*, 114977.
[7] Y. Zhang, H. Zhao, Y. Du, *J. Mater. Chem. A* **2016**, *4*, 7155.
[8] A. Kumar, S. N. Puravankara, *Mater. Today Energy* **2022**, *29*, 101115.
[9] L. S. Plashnitsa, E. Kobayashi, Y. Noguchi, S. Okada, J.-i. Yamaki, *J. Electrochem. Soc.* **2010**, *157*, A536.
[10] A. C. Radjendirane, D. K. Maurya, J. Ren, H. Hou, H. Algadi, B. B. Xu, Z. Guo, S. Angaiah, *Langmuir* **2024**, *40*, 16690.
[11] R. Thirupathi, V. Kumari, S. Chakraborty, S. Omar, *Progress Mater. Sci.* **2023**, *137*, 101128.
[12] X. Zhang, X. Rui, D. Chen, H. Tan, D. Yang, S. Huang, Y. Yu, *Nanoscale* **2019**, *11*, 2556.
[13] Z. Jian, Y. Sun, X. Ji, *Chem. Commun.* **2015**, *51*, 6381.
[14] M. K. Sadan, A. K. Haridas, H. Kim, C. Kim, G. B. Cho, K. K. Cho, J. H. Ahn, H. J. Ahn, *Nanoscale Adv.* **2020**, *2*, 5166.
[15] X. Rao, J. Wang, M.-A. Yang, H. Zhao, Z. Li, *APL Mater.* **2022**, *10*, 1.
[16] W. Duan, Z. Zhu, H. Li, Z. Hu, K. Zhang, F. Cheng, J. Chen, *J. Mater. Chem. A* **2014**, *2*, 8668.
[17] S. K. Pal, R. Saha, G. V. Kumar, S. Omar, *J. Phys. Chem. C* **2020**, *124*, 9161.
[18] M. Samiee, B. Radhakrishnan, Z. Rice, Z. Deng, Y. S. Meng, S. P. Ong, J. Luo, *J. Power Sources* **2017**, *347*, 229.
[19] A. Chakraborty, R. Thirupathi, S. Bhattacharyya, K. Singh, S. Omar, *J. Power Sources* **2023**, *572*, 233092.
[20] J. He, T. Tao, F. Yang, Z. Sun, Their Interfacial Chemistries Towards High-Rate Sodium-Ion Batteries., *ChemSusChem* **2022**, *15*, e202102522.
[21] F. Lalère, J. B. Leriche, M. Courty, S. Boulineau, V. Viallet, C. Masquelier, V. Seznec, *J. Power Sources* **2014**, *247*, 975.
[22] S. Dwivedi, S. Vasudevan, P. Balaya, *J. Mater. Chem. A* **2024**, *12*, 22867.
[23] R. Thirupathi, S. Sharma, S. Bhattacharyya, S. Omar, *J. Am. Ceram. Soc.* **2024**, *107*, 8328.
[24] Y. Noguchi, E. Kobayashi, L. S. Plashnitsa, S. Okada, J.-i. Yamaki, *Electrochim. Acta* **2013**, *101*, 59.
[25] W. Zhou, S. Wang, Y. Li, S. Xin, A. Manthiram, J. B. Goodenough, *J. Am. Chem. Soc.* **2016**, *138*, 9385.
[26] W. Zhou, Y. Li, S. Xin, J. B. Goodenough, *ACS Cent. Sci.* **2017**, *3*, 52.
[27] R. Thirupathi, R. P. Srivastava, B. Patankar, S. Bhattacharyya, M. Aman, S. Sharma, S. Omar, *Chem. Commun.* **2025**, *61*, 10931.
[28] L. S. Plashnitsa, E. Kobayashi, Y. Noguchi, S. Okada, J.-i. Yamaki, *J. Electrochem. Soc.* **2010**, *157*, A536.
[29] Y. Man, P. Jaumaux, Y. Xu, Y. Fei, X. Mo, G. Wang, X. Zhou, *Sci. Bull.* **2023**, *68*, 1819.
[30] Y. Wang, Z. Wang, J. Sun, F. Zheng, M. Kotobuki, T. Wu, K. Zeng, L. Lu, *J. Power Sources* **2020**, *454*, 227949.
[31] Y. Wang, Z. Wang, X. Xu, S. J. A. Oh, J. Sun, F. Zheng, X. Lu, C. Xu, B. Yan, G. Huang, L. Lu, *Nanomicro Lett.* **2024**, *16*, 254.
[32] H. Wang, Y. Sun, Q. Liu, Z. Mei, L. Yang, L. Duan, H. Guo, *J. Energy Chem.* **2022**, *74*, 18.
[33] A. A. Shindrov, K. V. Mishchenko, O. A. Podgornova, A. A. Shapovalova, N. V. Kosova, *Solid State Ionics* **2024**, *406*, 116485.
[34] R. P. Srivastava, S. Sharma, S. Bhattacharyya, P. Sharma, M. Aman, S. Omar, *Electrochimica Acta* **2025**, *540*, 147126.
[35] S. Sharma, S. Bhattacharyya, R. Thirupathi, R. P. Srivasatava, S. K. Jha, S. Omar, *ACS Appl. Energy Mater.* **2025**, *8*, 10984.
[36] S. Khurana, A. Chandra, *J. Polym. Sci. Part B: Polym. Phys.* **2017**, *56*, 207.
[37] K. Panwar, M. Jassal, A. K. Agrawal, *Particuology* **2015**, *19*, 107.
[38] L. Ran, S. Tao, I. Gentle, B. Luo, M. Li, L. Wang, R. Knibbe, *ACS Appl. Mater. Interfaces* **2021**, *13*, 39355.
[39] Y. Wang, S. Song, C. Xu, N. Hu, J. Molenda, L. Lu, *Nano Mater. Sci.* **2019**, *1*, 91.
[40] P. de Sainte Claire, *Macromolecules* **2009**, *42*, 3469.
[41] R. Huang, Y. Ding, F. Zhang, W. Jiang, C. Zhang, P. Yan, M. Ling, H. Pan, *J. Energy Chem.* **2022**, *75*, 504.
[42] S. Sarkar, T. K. Dutta, K. Jana, B. P. Mandal, A. Patra, *Small* **2025**, *21*, e2407756.
[43] M. C. Biesinger, *Appl. Surf. Sci.* **2022**, *597*, 153681.
[44] V. M. Mohan, V. Raja, A. K. Sharma, V. V. R. Narasimha Rao, *Ionics* **2006**, *12*, 219.
[45] E. Calabrò, S. Magazù, *Adv. Phys. Chem.* **2013**, *2013*, 1.
[46] B. L. Papke, M. A. Ratner, D. F. Shriver, *J. Electrochem. Soc.* **2019**, *129*, 1434.
[47] H. B. Sun, J. Z. Guo, Y. Zhang, T. Wei, Y. X. Zhou, L. L. Zhang, X. L. Wu, Y. Huang, W. Luo, *ACS Appl. Mater. Interfaces* **2019**, *11*, 24192.